JGR Solid Earth

RESEARCH ARTICLE
10.1029/2022JB024493

Power-Law Viscoelastic Flow of the Lower Accretionary Prism in the Makran Subduction Zone Following the 2013 Baluchistan Earthquake

Guo Cheng[1], William D. Barnhart[2], and Shaoyang Li[3]

[1]Department of Earth and Environmental Sciences, University of Iowa, Iowa City, IA, USA, [2]U.S. Geological Survey, Earthquake Hazards Program, Golden, CO, USA, [3]State Key Laboratory of Lithospheric Evolution, Institute of Geology and Geophysics, Chinese Academy of Sciences, Beijing, China

Key Points:

- We use finite element forward models to simulate the 6.5-year interferometric synthetic aperture radar deformation time-series following the 2013 Baluchistan earthquake
- Non-linear viscoelastic relaxation within the lower Makran accretionary prism dominates the post-seismic deformation
- The inferred flow-law parameters suggest low-temperature dislocation creep within the accretionary prism under fluid-saturated condition

Supporting Information:

Supporting Information may be found in the online version of this article.

Correspondence to:

G. Cheng,
guo-cheng@uiowa.edu

Citation:

Cheng, G., Barnhart, W. D., & Li, S. (2022). Power-law viscoelastic flow of the lower accretionary prism in the Makran subduction zone following the 2013 Baluchistan earthquake. *Journal of Geophysical Research: Solid Earth*, *127*, e2022JB024493. https://doi.org/10.1029/2022JB024493

Received 31 MAR 2022
Accepted 27 OCT 2022

Author Contributions:

Conceptualization: William D. Barnhart
Data curation: Guo Cheng
Formal analysis: Guo Cheng
Funding acquisition: William D. Barnhart
Investigation: Guo Cheng
Methodology: Guo Cheng, William D. Barnhart, Shaoyang Li
Project Administration: William D. Barnhart
Resources: William D. Barnhart, Shaoyang Li
Supervision: William D. Barnhart, Shaoyang Li
Visualization: Guo Cheng

Abstract Subduction zone accretionary prisms are commonly modeled as elastic structures where permanent deformation is accommodated by faulting and folding of otherwise elastic materials, yet accretionary prisms may exhibit other deformation styles over relatively short time scales. In this study, we use 6.5-year (2014–2021) Sentinel-1 interferometric synthetic aperture radar (InSAR) time-series of post-seismic deformation in the Makran accretionary prism of southeast Pakistan to characterize non-linear viscoelastic deformation within an active accretionary prism on short timescales (months to years). We constructed a series of 3-D finite-element models of the Makran subduction zone, including an accretionary prism, and constrained the elastic thickness of the upper wedge and the flow-law parameters (power-law exponent, activation enthalpy, and pre-exponential constant) of the lower wedge through forward model fits to the InSAR time-series. Our results show that the prism is elastically thin (8–12 km) and the non-linear viscoelastic relaxation of the deep portions of the prism alone can sufficiently explain the post-seismic surface deformation. Our best fitting flow-law parameters ($n = 3.76 \pm 0.39$, $Q = 82.2 \pm 37.73$ kJ mol^{-1}, and $A = 10^{-3.36\pm4.69}$) are consistent with triggering of low temperature dislocation creep within fluid-saturated siliciclastic rocks. We believe that the fluids necessary for this weakening originate from sedimentary underplating and/or the presence the hydrocarbons. The presence of power-law rheology within the lower wedge impacts the estimated plate coupling and the stress state in the subduction system, with respect to the conventional elastic wedge model, and hence should to be considered in future earthquake cycle models.

Plain Language Summary Following large earthquake ruptures, the Earth's surface can continue to deform for several years. The spatial and temporal pattern of this post-earthquake surface deformation is related to the material properties beneath the Earth's surface. By modeling this deformation, we are able to infer the mechanical behavior of the Earth at depth (i.e., whether it behaves like a solid or a fluid, or something in between), which has important implications for assessing the seismic hazard in the region. In 2013, a Mw7.7 earthquake occurred in the Makran accretionary prism in southern Pakistan. We use satellite images to measure and monitor the surface deformation 6.5 years following the earthquake. We find that this deformation is mainly caused by the viscoelastic relaxation, a flow-like behavior, of the lower prism material between 12- and 40-km depth. This behavior likely results from the high fluid content within the accretionary prism.

1. Introduction

Accretionary prisms are common geologic features in subduction zone environments whose long-term deformation are often described according to Mohr-Coulomb wedge theory (e.g., Dahlen et al., 1984; Davis et al., 1983; Wang & Hu, 2006), which invokes elastic mechanics with frictional yielding to explain the relationships between the wedge taper, basal friction, and internal strength of the wedge. Where present, accretionary prisms are the shallowest portion of the hanging wall in accretionary subduction zones, and the mechanics of accretionary prisms across varying time periods may influence shallow megathrust rupture characteristics, such as tsunamigenesis. Similarly, subduction zone coupling models, which rely on geodetic measurements made within and inboard of the accretionary prism, often invoke homogeneous elastic deformation models (Bevis et al., 2001; Chlieh et al., 2011; Moreno et al., 2010). If accretionary prism undergo viscous deformation on relatively short time scales, then models of subduction zone hazard and behavior based on an assumption of elastic deformation may be biased.

Writing – original draft: Guo Cheng
Writing – review & editing: Guo Cheng, William D. Barnhart, Shaoyang Li

Several studies showed non-elastic deformation over time-scales of an earthquake cycle or shorter within the accretionary prism or mantle wedge. Sun et al. (2014) showed viscoelastic relaxation within the upper mantle following the 2011 Tohoku-oki earthquake. Peña et al. (2020) showed power-law relaxation within the lower continental crust and upper mantle of the Chilean subduction zone after the 2010 Maule earthquake. Peterson et al. (2018) characterized the post-seismic surface deformation of the 2013 Baluchistan strike-slip earthquake within the Makran accretionary prism of southern Pakistan and found that the observed post-seismic deformation transient could be explained to a first-order by non-linear viscoelastic relaxation within the accretionary prism. Of all these studies, only in Japan and Pakistan were the geodetic observations (sea floor global positioning system (GPS) and interferometric synthetic aperture radar (InSAR) time-series, respectively) available within the accretionary prism, which is a relatively rare occurrence given most accretionary prisms are under water. Given the current rarity of such observations of post-seismic deformation in the shallow subduction zone, detailed interrogation of these post-seismic transients is critical to new understanding of accretionary wedge mechanics.

The Makran subduction zone, located in southeast Iran and southwest Pakistan, accommodates northward subduction of the Arabia oceanic plate beneath the Eurasia continental plate at 3.8–4.0 cm/year (DeMets et al., 2010, Figure 1). The Makran accretionary prism (MAP) is an east-west trending (~1,000 km) wedge with, advantageously for geodetic observations, a 150–200 km wide region that is exposed subaerially. The MAP consists primarily of siliciclastic turbidite sequences that exhibit significant evidence of fluid over-saturation attributed to sedimentary underplating (Burg, 2018; Fowler et al., 1985; Fruehn et al., 1997; Platt et al., 1985). Recent GPS and InSAR investigations suggest that the megathrust is strongly coupled at the coastline and capable of producing ~M_W8.8 earthquakes (Frohling & Szeliga, 2016; Lin et al., 2015). Historically, the Makran hosted several large (suspected or observed $M_W > 7.0$) megathrust earthquakes (Figure 1), including the 1,483 event in western Makran, the 1,765 event in easternmost Makran, two coastal events in 1851 and 1864 in eastern Makran, and the 1945 M_W8.1 event near Pasni, followed by a large aftershock in 1947 (Byrne et al., 1992; Heidarzadeh & Satake, 2015). Some of these earthquakes were tsunamigenic and impacted large cities throughout the Arabian Sea and Indian Ocean, including megacities of Karachi (currently having 21+ million population) and Mumbai (18+ million) (Byrne et al., 1992; Jaiswal et al., 2009).

Several previous studies have suggested that the MAP is mechanically weak. The Arabian plate subducts at a shallow angle, and the surface slope of the MAP is similarly shallow dipping. Under Mohr-Coulomb wedge theory, these factors indicate an internal frictional coefficient smaller than 0.05, which in part indicated elevated pore fluid pressures (Barnhart et al., 2014; Dahlen et al., 1984). At the same time, mud volcanos, high porosity evident in seismic surveys, and dissolution structures observed in the field indicate the presence of substantial fluid in the accretionary prism that reduces the strength of rocks within the wedge (Fowler et al., 1985; Fruehn et al., 1997; Snead, 1964; Wiedicke et al., 2001).

On 24 September 2013, a M_W7.7 strike-slip earthquake occurred within the sub-aerial portion of the MAP (Avouac et al., 2014; Barnhart et al., 2014; Jolivet et al., 2014) (Figure 1). InSAR time-series observations that began 15 months after the earthquake showed an extensive and ongoing post-seismic transient that was first described by Peterson et al. (2018). In that preliminary study, Peterson et al. showed that, to a first order, the transient could be explained by non-linear viscoelastic relaxation within a layered half-space without the presence of afterslip. They estimated the power-law exponent ($n = 3.5$) of the lower MAP with an effective viscosity of 10^{17}–10^{18} Pa·s. They hypothesized that the non-linear rheology reflects low temperature creep processes. In this study, we aim to build on and improve the work done by Peterson et al. in several ways. First, we extended the temporal aperture of surface displacement observations from 2.5 to 6.5 years to retrieve the post-seismic surface deformation transient that may constrain the viscoelastic relaxation process more tightly. Second, while the previous study used a simplified 4-layer model to represent the subduction zone structure without lateral heterogeneities, we invoked a more realistic subduction zone model with geophysically constrained slab geometry, Moho depth, and material properties to minimize biases introduced by the simple layered model. Third, we applied a lab-derived constitutive relationship to solve for the non-linear viscoelastic response and the flow-law parameters of the lower wedge material, whereas Peterson et al. assumed a linear Maxwell body to approximate the non-linear response.

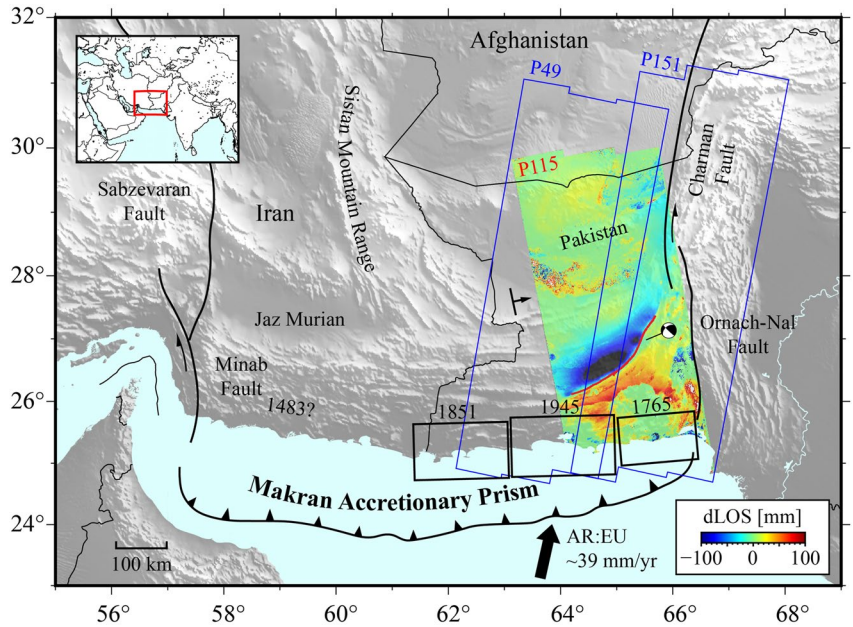

Figure 1. General setting and simplified structural map of the Makran subduction zone, modified from Burg (2018), and 6.5-year cumulative (starting Oct. 2014) line-of-sight displacements derived from the ascending (Path 115) path of Sentinel-1 SAR imagery. The color scales saturate at ±100 mm. Black arrows indicate the LOS directions. Positive value indicates increasing LOS (away from the satellite). Blue boxes outline the footprints of two descending (Path 151 and 49) Sentinel interferograms used in this study. The red line indicates the rupture trace of the 2013 Mw7.7 Baluchistan earthquake. Black rectangles indicate maximum estimated rupture areas for historic earthquake events (Byrne et al., 1992). Plate motion of Arabia relative to Eurasia (AR:EU) is shown by black arrow (DeMets et al., 2010). Structures and images are overlain on 30 m SRTM DEM shaded relief.

2. Data and Methods

2.1. InSAR Time-Series Processing

We generated a 6.5-year (October 2014–March 2021) Sentinel-1 InSAR time-series from three different satellite paths (one ascending, two descending) spanning the Baluchistan earthquake post-seismic transient (Figure 1; Figures S1 and S2 in Supporting Information S1). Unfortunately, we were unable to constrain the early post-seismic deformation following the September 2013 earthquake because of a lack of SAR observations in the first 13 months following the earthquake. Each SAR acquisition was paired with the next three acquisitions to form interferometric pairs using the stack processing tools within the JPL/Caltech ISCE processing package (Rosen et al., 2004). We removed topography-related phases with the 30-m Shuttle Radar Topography Mission (SRTM) digital elevation model. After generating stacks of interferograms from each path, we inverted the line-of-sight (LOS) displacements for the displacement time-series of each pixel using the Miami InSAR Time-series Software in Python (MintPy, Zhang et al., 2019). We applied no atmospheric corrections to the time-series because a lack of continuous GPS observations in the region of interest did not allow us to validate the atmospheric corrections.

We then fit a logarithmic decay function to the time-series of each pixel using a minimum root mean square (RMS) grid search method to generate a smoothed displacement time-series:

$$d_{\mathrm{LOS}} = a \log(1 + t/\tau) \quad (1)$$

where d_{LOS} is the LOS displacement in millimeter, t is time since the earthquake rupture in years, and a and τ are the parameters we search for. For the purposes of comparing the time-series to predictions from a finite element model, we resampled the smoothed time-series onto 30 equally-spaced dates within the shared temporal window of the three satellite paths.

2.2. Finite-Element Modeling

We constructed 3-D finite-element models of the Makran subduction zone (Figure 2). Different from Peterson et al. (2018), which assumed a simplified four-layer wedge structure, we constructed the Makran subduction zone and accretionary prism in *Coreform-Cubit* (https://coreform.com/) using a geophysically constrained geometry. While our subduction zone geometry represents more details than Peterson et al. (2018), it does not incorporate complex upper plate geometry, such as the sequential folding and faulting within the accretionary forearc. Therefore, our model geometry is a first-order approximation of the complex Makran accretionary prism. The structure of our 3-D model consists of four domains (Figure 2): (a) an elastic upper wedge where the 2013 Mw7.7 earthquake occurred; (b) a viscoelastic lower wedge that extends to the dipping slab interface to a maximum depth of 40 km, which is the Moho depth reported in this region (Abdollahi et al., 2018; Maggi et al., 2000; Shad Manaman et al., 2011); (c) a 30 km thick elastic Arabic oceanic slab with surface curvature derived from the Slab2 model (Craig & Copley, 2014; Hayes et al., 2018); and (d) a viscoelastic oceanic and continental mantle at depths greater than the previously described domains. We then used the open-source *PyLith* finite element modeling package to assign material properties to different domains and derive the post-seismic forward simulations (Aagaard et al., 2013). For simplicity, each domain is assumed to be homogeneous. Table S1 in Supporting Information S1 summarizes the material properties assigned to these domains. We set free displacement boundary condition for the ground surface. For the northern/southern and eastern/western boundaries, we set roller conditions where displacements are fixed in normal direction but free in tangential directions.

Here we design a two-step approach to constrain the source of the viscoelastic relaxation at depth. We first conducted a series of forward model tests to estimate the thickness of the accretionary prism elastic layer (akin to the elastic-crystal plastic transition (ECPT)). We then constrained the flow-law parameters of the Makran lower wedge with non-linear FEM forward simulations.

2.2.1. Estimation of the Elastic-Crystal Plastic Transition (ECPT) Depth

We varied the ECPT depth in our finite element mesh from 4 to 20 km in 4 km increments. We prescribed the co-seismic slip distribution from Jolivet et al. (2014) onto the Hoshab fault, and simulated the post-rupture deformation for 10 years. We evaluate the dependence of model fit on ECPT depths with the lower wedge exhibiting both linear Maxwell and non-linear power-law rheology. For the Maxwell model, we kept the elastic properties constant while assigning varying linear Maxwell viscosities from 0 to 4e+19 Pa·s (Table S1 in Supporting Information S1). For power-law rheology, laboratory experiments suggest the following flow law:

$$\dot{\varepsilon} = A\sigma^{n} e^{(-Q/\mathrm{RT})} \tag{2}$$

where $\dot{\varepsilon}$ is strain rate (s^{-1}), A is a pre-exponential factor ($MPa^{-n}\ s^{-1}$), σ is the differential stress (MPa), n is the power-law exponent, Q is the activation energy (kJ mol^{-1}), R is the universal gas constant (J mol^{-1} K^{-1}), and T is temperature (K), which is depth-dependent following a regional geothermal gradient of 10°C/km (Khan & Raza, 1986; Peterson et al., 2018). For each ECPT depth, we vary the power-law parameters of the lower wedge with: n ranging from 3 to 4; Q ranging from 50 to 140 kJ mol^{-1}; and A ranging from 10^{-8} to 10^{7} $MPa^{-n}\ s^{-1}$, in total of 1,260 models (Table S1 in Supporting Information S1).

To evaluate the fit of forward simulations to the InSAR time-series, we projected the 3-D surface displacement time-series predicted from the finite element models to the radar LOS directions of each satellite path. For each path, we shifted the modeled time-series to make it have zero displacement on the first date of InSAR acquisition. We then resampled the predicted time-series at the same 30 dates as the InSAR time-series. Lastly, we calculated the mean RMS misfit (mRMS) between the predicted and observed time-series on a pixel-by-pixel basis:

$$\chi^{2} = \frac{1}{n_d} \bullet \frac{1}{n_p} \sum_{i=1}^{n_d} \sum_{j=1}^{n_p} \left[(d_{ij} - m_{ij})^{2} \right] \tag{3}$$

where χ^2 is the misfit squared, n_d is the number of dates, n_p is the number of pixels, and d_{ij}, m_{ij} are the line-of-sight displacements for the ith pixel on jth date for data and model, respectively. We aim to find out at which ECPT depth does the model produce the minimum mRMS error.

Since each path contains different level of tropospheric or ionospheric noise, and each path's coverage of the post-seismic deformation varies as well (Figures S1–S3 in Supporting Information S1), we normalized the mRMS distributions and applied variable weighting for each path. Although it remains difficult to quantitatively

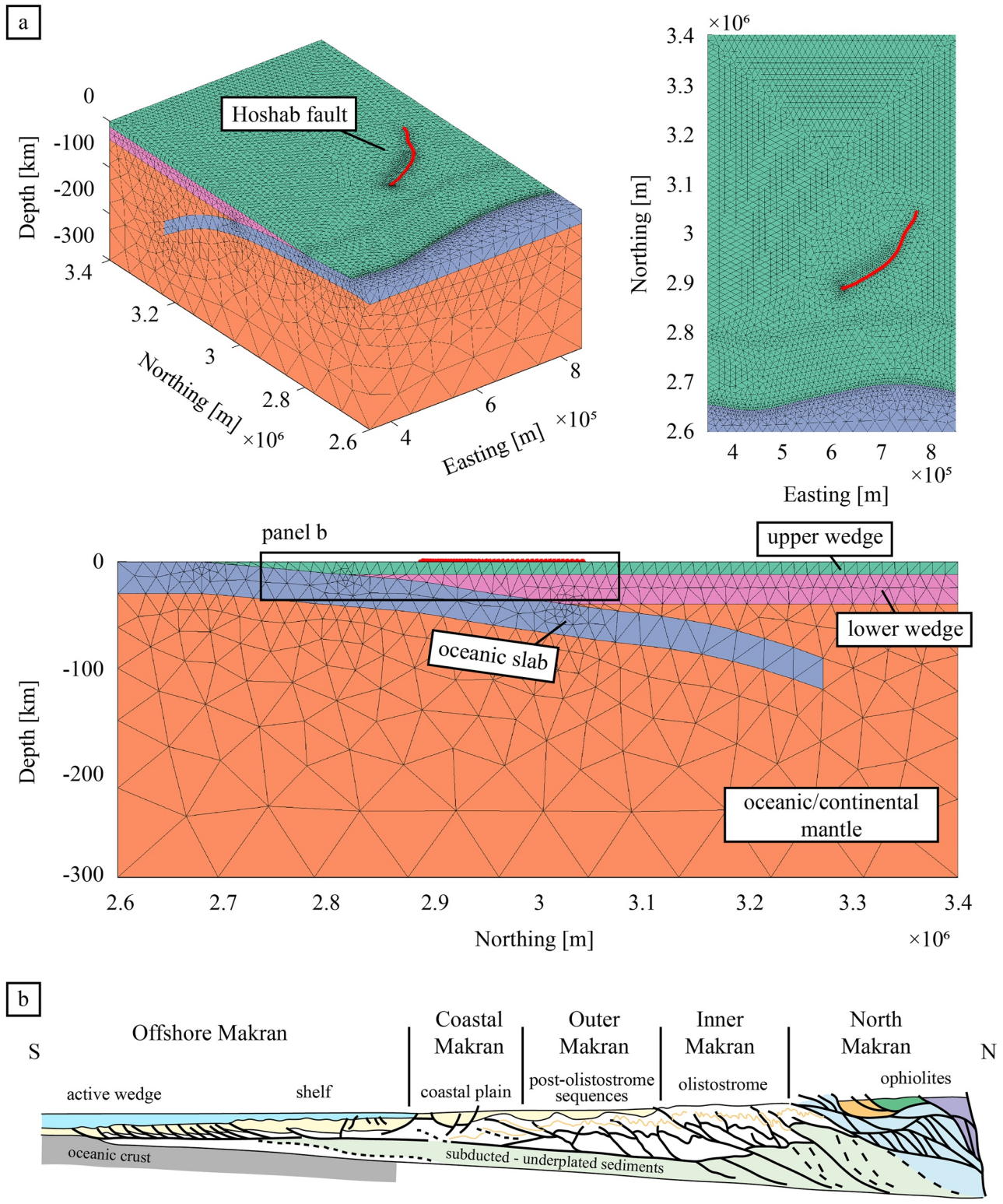

Figure 2.

assess the weighting of spatial coverage and noise content within each path on the fit of our forward models, we employed a guided trial and error approach to find the optimal weights to the mRMS distribution of each path. We assigned the weight on the ascending path larger than the two descending paths as it covers all of the post-seismic deformation signal and has relatively low noise content in the vicinity of the Hoshab fault. Additionally, for the

ascending path, the post-seismic surface displacements are relatively in the direction of the satellite's range, along which the radar sensors are most sensitive to displacements. We also kept the weights on the two descending paths the same. As a result, we found that a weight of 0.6 on the ascending path and 0.2 on each of the descending paths explain the observation well.

2.2.2. Post-Seismic Relaxation Modeling With Non-Linear Lower Wedge Rheology

After estimating the ECPT depth, we conducted forward simulations of 10-year of post-seismic 3-D deformation of the 2013 Baluchistan earthquake assuming non-linear power-law rheology applied to the lower viscoelastic wedge: While keeping the material properties of other domains the same as before, we expand the power-law parameters of the lower wedge with: n ranging from 3 to 5; Q ranging from 10 to 200 kJ mol^{-1}; and A ranging from 10^{-15} to 10^{13} MPa^{-n} s^{-1}, in total of 6,820 different rheology models (Table S1 in Supporting Information S1).

For each of the 6,820 resulting forward models, we calculated the mRMS misfit between the predicted and observed LOS time-series along each satellite paths (Equation 3). We normalized the mRMS distribution and assigned the same weighting as we used in the previous step for each satellite path (0.6 for the ascending path, and 0.2 for the descending paths). Given the potential non-linear trade-offs between the three unconstrained variables and large parameter spaces, we do not expect to find the one single rheology model that best fits the observations. Instead, we aim to find a range of models that provide good fits based on both the weighted mRMS (WmRMS) misfit and visual inspection of the spatial and temporal fits between the predicted and observed time-series. To quantify the weighted mRMS distribution, we defined a simple criterion, in which we selected 5% of all model that have the lowest WmRMS values, and then calculated the mean and 1-σ uncertainties of each flow-law parameter. We also aim to explore the control of each variable on the spatial and temporal patterns of the post-seismic surface displacements.

3. Results

3.1. Estimation of the ECPT Depth

Figure 3 shows the comparison between the best-fitting Maxwell and power-law models at each ECPT depth for the Jolivet slip model. Overall, the normalized WmRMS distributions suggest that for both models, the forward simulations yield the best fit (minimum WmRMS) at an ECPT depth between 8 and 12 km. However, the power-law best-fitting models yield lower WmRMS than their Maxwell counterparts. For each rheology model, the fit between the predicted and observed time-series varies for different InSAR viewing geometries. In general, for both path 115 and 151, fits show that the best fit occurs at an ECPT depth between 8 and 12 km (Figures S4a, S4b, S4d, and S4e in Supporting Information S1). For path 49, we do not observe apparent correlation between ECPT depth, lower wedge viscosity, and model fit (Figures S4c and S4f in Supporting Information S1), which likely results from relatively high noise content in the InSAR time-series of this path. As a result, we believe that the boundary between the elastic and crystal-plastic deformation occurs at 8- to 12-km depth in the Makran region, and the non-linear power-law rheology explains the lower wedge behavior better than the linear Maxell model. Following this estimation, we then fixed the thickness of the elastic upper wedge to be 12 km in our later non-linear forward simulations (Figure 2).

3.2. Post-Seismic Relaxation Modeling With Non-Linear Lower Wedge Rheology

Figure 4 shows the normalized WmRMS distribution for all 6,820 forward models at each InSAR viewing geometry. Models with low WmRMS values (5% of all models) yield a lower wedge rheology of (1-σ): $n = 3.76 \pm 0.39$, $Q = 82.2 \pm 37.73$ kJ mol^{-1}, and $A = 10^{-3.36 \pm 4.69}$. The model with the minimum mRMS yields: $n = 3.6$,

Figure 2. (a) An example of Makran subduction zone geometry (12 km of the upper wedge thickness) and finite element mesh. Green domain: upper wedge. Blue domain: oceanic slab. Pink domain: lower wedge. Orange domain: oceanic and continental mantle. Red line: Hoshab fault trace. Note that in the third panel, within the upper wedge and the frontal portion of the lower wedge, the mesh is of only one-element thickness. This is because the third panel only shows mesh element distribution on the easternmost boundary of the domain. In the domain interior, the element size becomes finer as its distance to the Hoshab fault decreases. At the fault plane, the element size is on average 1-km in diameter, resulting in approximately 12 layers of mesh elements. (b) General cross-section (box in a) of the Makran accretionary prism modified after (Burg, 2018). Folded orange line: Eocene-Lower Miocene sediments. Pale yellow: Upper Miocene-Quaternary deposits. Orange: granitoids, lavas and sediments. Light blue: low grade metamorphic rocks including blue schist. Green and Purple: ophiolite packages.

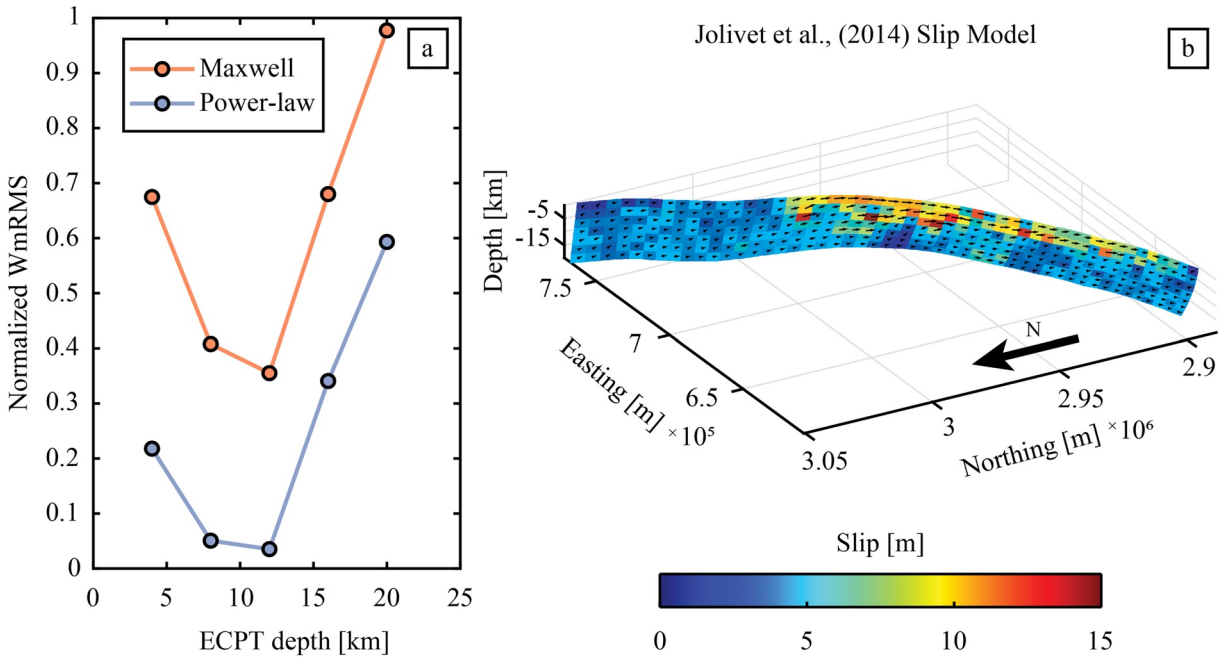

Figure 3. (a) Normalized weighted mean RMS (WmRMS) between the best-fitting models (circles) and data at various ECPT depth assumptions (4, 8, 12, 16, and 20 km) for Maxwell lower wedge rheology (orange line), power-law rheology (blue line). (b) Jolivet et al. (2014) co-seismic slip distributions.

$Q = 70$ kJ mol^{-1}, and $A = 10^{-4.8}$. We also observe a positive correlation between log(A) and Q (Figure 4a). Figures S5–S7 in Supporting Information S1 show mRMS distributions for each path 115, 151, and 49, respectively.

Figure 5 shows the cumulative post-seismic deformation predicted from the minimum WmRMS model for all three satellite viewing geometries and their residuals to the InSAR observations. For both path 115 and path 151, the forward model predicts most of the post-seismic deformation signals following the 2013 Baluchistan earthquake, in both spatial (Figures 5a–5d) and temporal (Figures 5g and 5h) domains, indicating that viscoelastic relaxation alone can explain the post-seismic transient. We observe near-field residuals in the ascending path. While some of these residuals results from continuous fault creep that has been identified in previous studies (Boxes A and B in Figure 5a, Fattahi, 2015; Peterson et al., 2018), the origin of the others remains uncertain. We believe that the coherent near-field residuals likely arise from over simplification of near-surface structure and slip in both our FEM and the input slip distribution. Additionally, we show the predicted cumulative displacements in the east, north, and upward directions (Figure S8 in Supporting Information S1).

To illustrate the effects of non-linear lower wedge rheology on the post-seismic deformation, we compared results from the best-fitting Maxwell model from the ECPT estimation tests (η = 8.4e+18), and the power-law model with the minimum WmRMS (n = 3.6, Q = 70 kJ mol^{-1}, and $A = 10^{-4.8}$). Figure 6 shows the predicted post-seismic time-series of these two models in the temporal domain for selected locations near the Hoshab fault. We observed, to a first order, that the power-law model captures the logarithmic decay pattern in the post-seismic InSAR time-series, whereas the Maxwell model exhibit a linear tend in the time-series and do not match the temporal signal decay. Recalling the results from the ECPT estimation, the power-law models yield overall lower WmRMS the Maxwell models (Figure 3). Therefore, we conclude that power-law rheology in the lower accretionary prism better explains the observed post-seismic deformation.

We further explore the temporal evolution of viscosity for the best-fitting power-law model. We compute the transient effective viscosity of the lower wedge following (Freed & Bürgmann, 2004): $\eta = \sigma^{(1-n)} e^{(Q/\mathrm{RT})}/2A$, where differential stress σ is defined as the absolute difference between the maximum and minimum principal stresses. As shown in Figure 7, immediately following the rupture, high differential stress beneath the Hoshab fault results in a low viscosity (on the order of 10^{16} Pa·s) zone in the lower wedge and parallel to the slab-wedge interface. As the stress relaxes, the effective viscosity gradually increases and reaches ~10^{18} Pa·s after 10 years. These stress- and time-dependent viscosity variations have been observed following other earthquakes under different

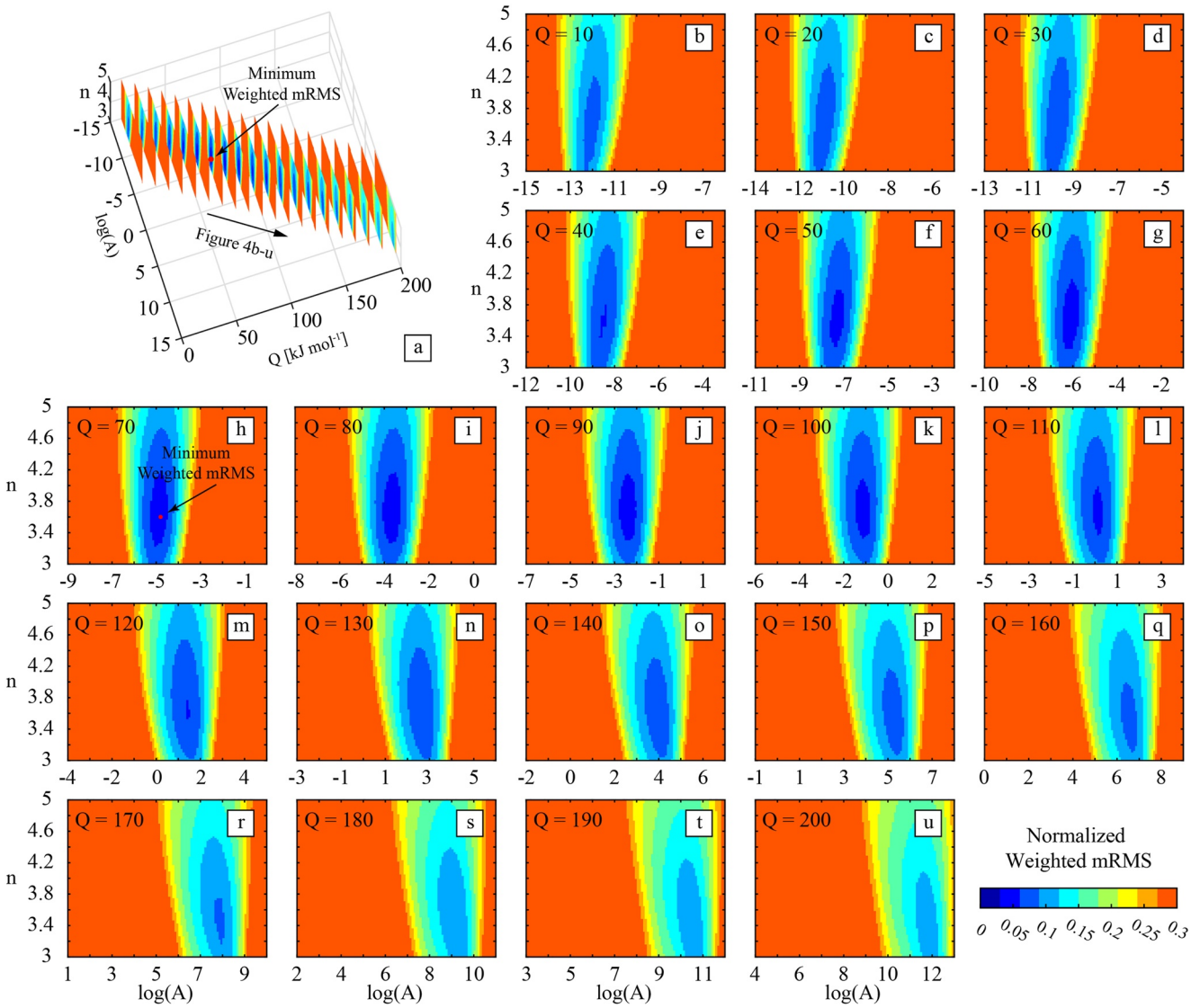

Figure 4. (a) Normalized weighted mRMS distributions for all FEM forward models of different *A* (pre-exponential constant), *Q* (activation enthalpy), and *n* (power-law exponent) combinations. (b–u) Expanded plots of (a), each of which shows the normalized weighted mRMS distribution with a constant *Q* value. The red circles indicate the model with the minimum weighted mRMS.

tectonic settings, such as the 1992 Landers, 1999 Hector Mine, 2002 Denali, 2008 Wenchuan earthquakes, 2010 Maule, and 2011 Tohoku earthquakes (Freed & Bürgmann, 2004; Freed et al., 2006; Muto et al., 2019; Peña et al., 2020; Zhu et al., 2022). Additionally, we conduct several tests in which we reduce the Young's modulus (*E*) of the oceanic slab (From 120 GPa to 100, and 80 GPa) and the viscosity of the continental/oceanic mantle (From 10^{20} to 10^{19} Pa·s), to investigate whether the stiffness of the subducting slab or mantle viscosity affects the spatial and temporal variations in the low viscosity zone. We do not observe apparent change in effective viscosity for these models with weaker oceanic slab or less viscous mantle, which indicates that our choice of slab and mantle rheology does not impact our overall modeling results (Figures S9, S10, and S11). Based on these observations, we infer that the 2013 Baluchistan earthquake rupture likely stresses the lower Makran wedge, which creates a transient ductile zone along the plate interface (~20 km depth; Byrne et al., 1992; Jackson & McKenzie, 1984).

The viscoelastic relaxation of materials within the ductile zone along the subducted slab contributes to the surface deformation we observed with InSAR, particularly in the later years of our study (~5 years after origin) when the effective viscosity in the broader accretionary prism has returned to a high viscosity state (Figure 7). In a recent study, Lv et al. (2022) conducted afterslip inversions of the 2013 Baluchistan post-seismic InSAR time-series on

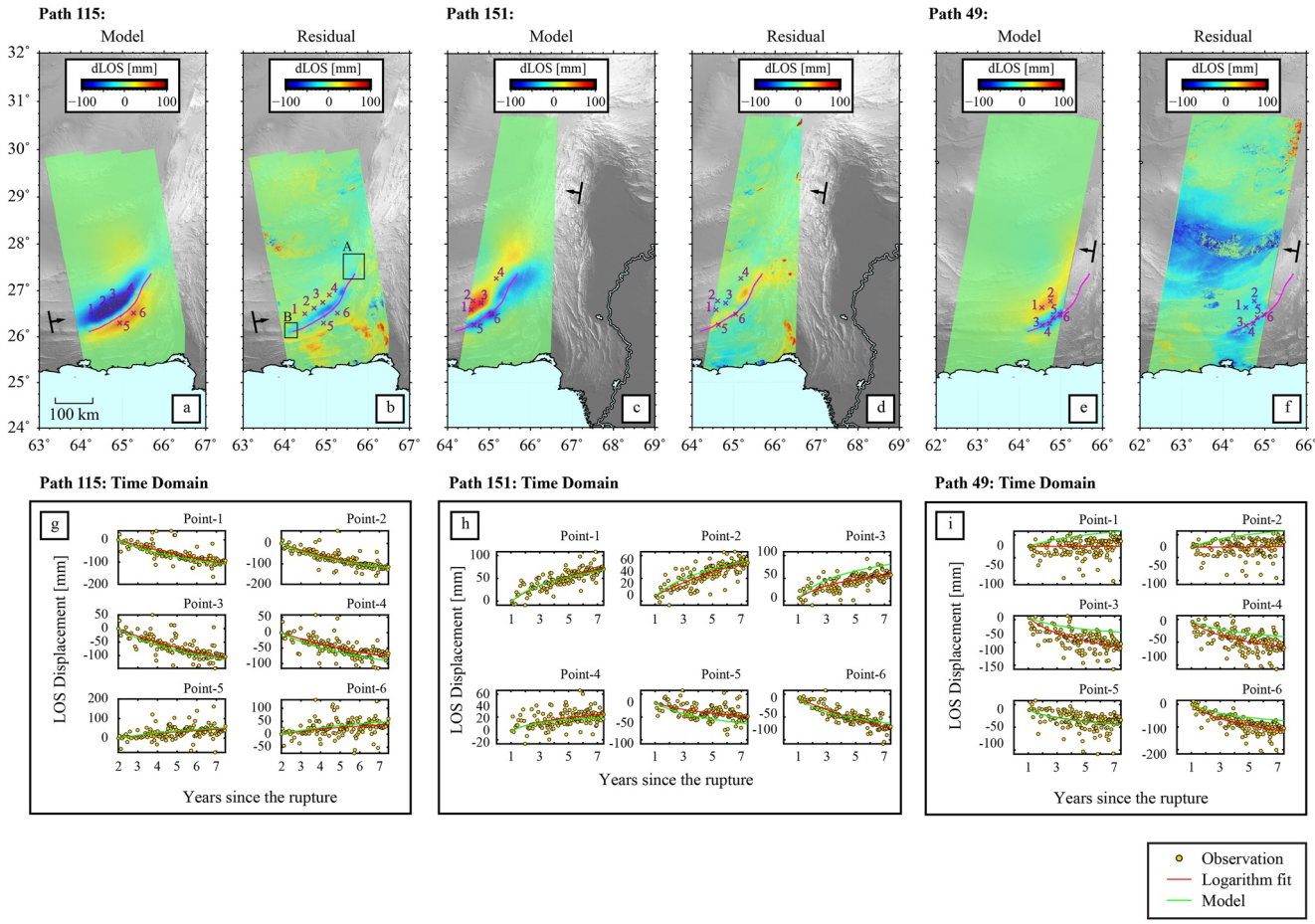

Figure 5. (a–f) Forward-modeled post-seismic surface displacements time-series ($A = 10^{-4.8}$ MPa^{-n} s^{-1}, $Q = 70$ kJ mol^{-1}, $n = 3.6$), and their last-date residuals to the InSAR time-series along path 115, 151, and 49. The color scales saturate at ±100 mm. Pink solid line indicates the Hoshab fault. Crosses and numbers correspond to selected locations of time-series plots shown in (g–i). Box A and B in (b) highlight residual signals likely resulting from continuous fault creep (see text). (g–i) Pixel-wise surface displacement time-series at locations shown in the upper panel for path 115, 151, and 49, respectively. Yellow circles: raw InSAR time-series. Red lines: logarithm fits of raw time-series; Green lines: modeled time-series. The time window for each panel spans from October 2014 to March 2021. Zero displacement is set at the date of first SAR acquisition.

different fault geometries. They argued that post-seismic deformation apparent in InSAR could be explained by aseismic afterslip on the Makran slab interface. Our results, which do not require or allow for the occurrence of frictional afterslip, indicate that the zone of low effective viscosity along the subduction zone interface is located where Lv et al. (2022) mapped afterslip and persists—therefore relaxing—throughout the InSAR observation period. Given that our modeling results fit the same observations well, we argue that frictional afterslip on the megathrust interface is not a unique mechanism to describe the observed surface deformation. Furthermore, our modeling results indicate that frictional afterslip is not required to explain the InSAR-observed post-seismic deformation signal. The occurrence of viscoelastic relaxation in a slab-parallel ductile zone may be an important component of post-seismic deformation in other subduction zone earthquakes, and may lead to misinterpretation of post-seismic mechanisms.

4. Discussion

Our analysis is consistent with the work of Peterson et al. (2018) which proposed that the post-seismic surface deformation can be explained by the viscoelastic relaxation of a weak lower Makran accretionary prism, above the subducted slab. This viscous lower wedge resides underneath an 8- to 12-km thick elastic upper wedge and extends to the interface with the rigid subducted slab. The lower wedge material exhibits a bulk power-law rheology with $n = 3.76 \pm 0.39$, $Q = 82.2 \pm 37.73$ kJ mol^{-1}, and $A = 10^{-3.36 \pm 4.69}$. Other flow laws, such as bi-viscous

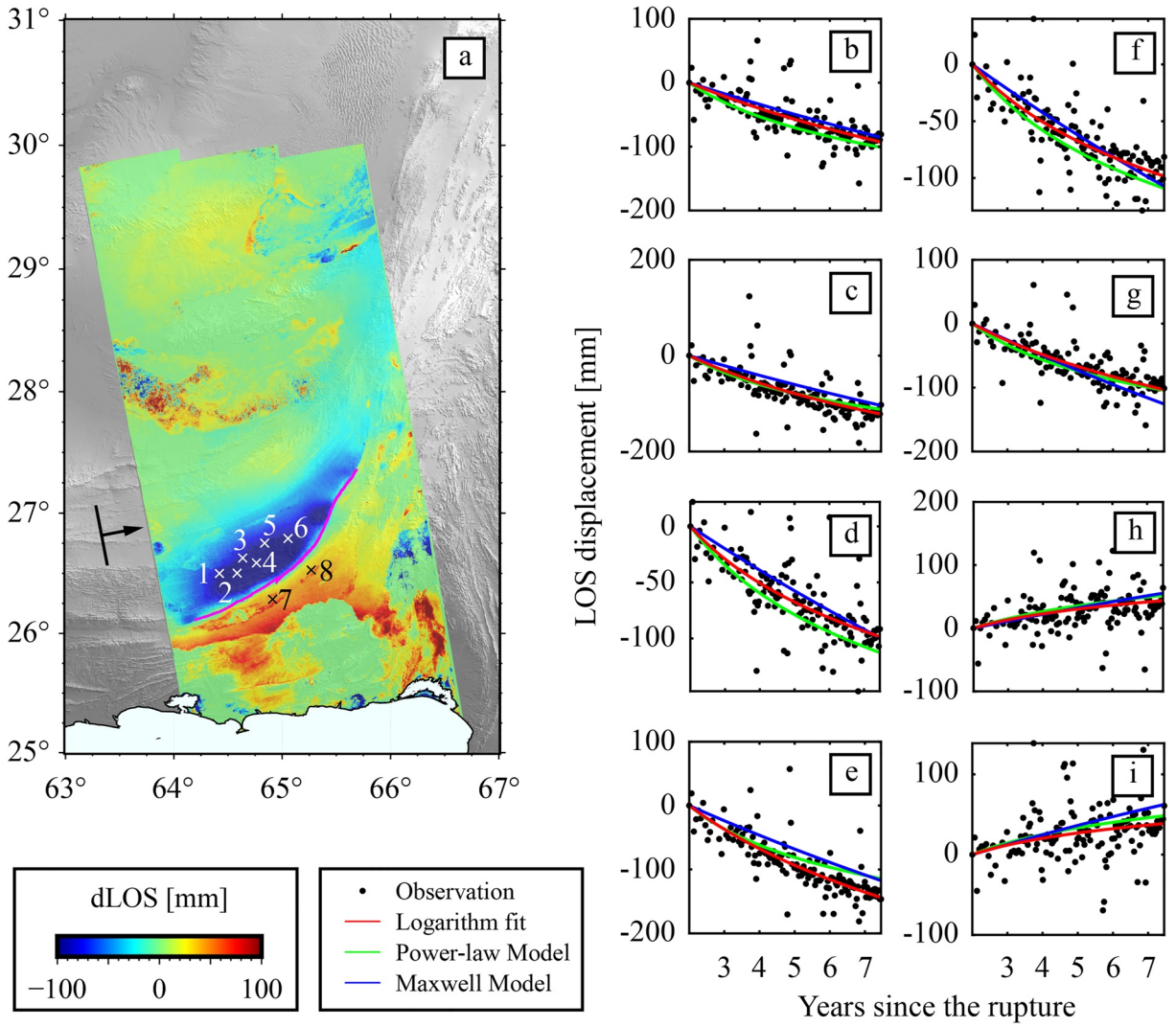

Figure 6. Comparison between InSAR observations and time-series predictions from the best-fitting power-law and Maxwell model. (a) 6.5-year InSAR time-series with selected locations (white and black crosses). Numbers (1–8) correspond to plots on the right (b–i). (b–i) Observed and predicted LOS displacement time-series in the temporal domain at location in (a). Black dots: raw InSAR time-series. Red lines: logarithm fits of raw time-series; Green lines: predicted time-series from the best-fitting power-law model ($n = 3.6$, $Q = 70$ kJ mol^{-1}, and $A = 10^{-4.8}$). Blue lines: predicted time-series from the best-fitting Maxwell model ($\eta = 8.4e{+}18$).

Burger's rheology, might also be able to fit the decaying post-seismic deformation as well, as it invokes both transient and steady-state viscosities. However, these possibilities are not tested in this study as we believe that using power-law rheology allows more direct comparison between model-derived material properties and field geological evidence. Similar post-seismic viscoelastic responses were observed in other plate boundary settings such as southern California, western Chile, western Sumatra and eastern Tibet (Freed & Bürgmann, 2004; Peña et al., 2020; Pollitz et al., 2006; Ryder et al., 2007; Yamasaki & Houseman, 2012). Additionally, based on predictions from numerical wedge evolution models by previous studies, our interpretation of a layered accretionary prism rheology is consistent with field observations in the Makran region. For instance, in a numerical sandbox model, Wenk and Huhn (2013) showed that a viscous layer within an accretionary wedge would lead to the formation of a stable detachment, decoupling the brittle strata above and viscous materials below. This is in consistent with the field observations that sequence of landward dipping faults (including the Hoshab) terminate at a common unconformity at about 10-km depth (Ellouz-Zimmermann et al., 2007), within our estimation of the ECPT depth in the region.

Our estimates of the lower wedge flow-law parameters (n, Q, and A) suggest that the dominating deformation mechanism that controls the viscoelastic behavior of the Makran wedge is likely dislocation creep ($n > 1$)

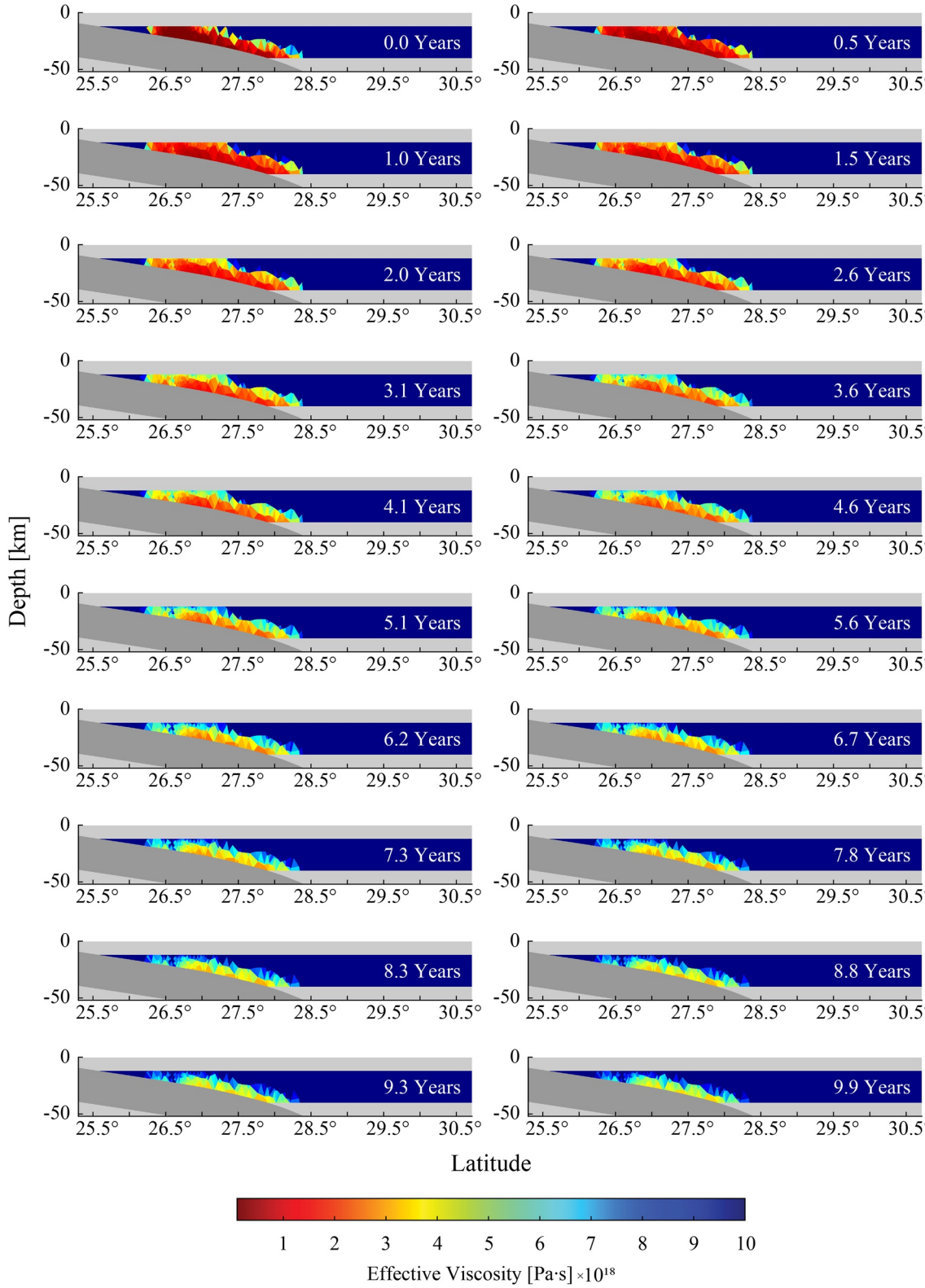

Figure 7. Temporal evolution of the effective viscosity within the Makran lower wedge for the best-fitting power-law model. Mantle wedge viscosity: 10^{20} Pa·s. Gray colored areas: upper wedge, oceanic slab, and mantle adjacent to the lower wedge domain. Time stamps in each panel represent time since the rupture.

(Bürgmann & Dresen, 2008; Freed & Bürgmann, 2004; Hirth & Kohlstedt, 2003; Rybacki et al., 2006). This type of crystal plastic deformation usually becomes dominant under comparatively high-temperature condition (e.g., 300°–400°C for quartz, 450°–600°C for feldspar, Passchier & Trouw, 2013). However, in an accretionary prism, the geothermal gradient is suppressed due to the presence of the "cold" oceanic lithosphere. In the case of the Makran, the geothermal gradient is estimated to be in the range of 10°–20°C/km (Khan & Raza, 1986; Peterson et al., 2018), which yields a temperature of 120°–240°C at our estimated ECPT depth. Under this thermal condition, brittle fracturing or pressure solution are usually the dominant deformation mechanisms instead of dislocation creep within minerals of partially metamorphosed sedimentary rocks (Burkhard, 1990; Kennedy & Logan, 1998; Stipp et al., 2002; van Daalen et al., 1999).

The occurrence of low-temperature dislocation creep within the Makran accretionary prism that we hypothesize is broadly consistent with the observed and inferred presence of fluid-saturated siliciclastic materials in the MAP. Lithologically, the primary rock types in the Makran region are quartzolithic sandstones and mudstones with minimal evidence of carbonates (Ahmed, 1969; Burg, 2018; Fruehn et al., 1997; Harms et al., 1984). The MAP is additionally underlain by ∼12 km thick of underplated sediments that introduce a fluid source (Platt et al., 1985). The presence of fluids in the Makran is evidenced by field observations of dissolution structures, mud volcanoes, and high porosity from seismic surveys of coastal Makran (Fowler et al., 1985; Fruehn et al., 1997; Schlüter et al., 2002; Snead, 1964; Wiedicke et al., 2001).

These geologic conditions in turn provide a means of comparison to laboratory tests of quartz deformation mechanisms. Dislocation creep in dry quartz requires temperatures of 300°–400°C that are too high for the MAP, but this temperature can be reduced in the presence of fluids (Griggs & Blacic, 1965; Luan & Paterson, 1992; Post et al., 1996). Laboratory hot-pressing experiments on synthetic quartz aggregates or natural quartzite reveal that the activation energy (Q) of quartz is in the range of ∼100–200 kJ mol^{-1} (Gleason & Tullis, 1995; Hirth et al., 2001; Luan & Paterson, 1992), which overlaps with our estimation of activation energy from the forward simulations (82.2 ± 37.73 kJ mol^{-1}). Pre-exponential factor (A) estimated from our forward modeling ($10^{-3.36\pm4.69}$) is higher than the experimentally derived value (∼10^{-12}, Hirth et al., 2001). This higher A value we estimate may reflect the increase in water fugacity, which is embedded in A, as a result of fluid saturation (Jaoul et al., 1984; Luan & Paterson, 1992; Post et al., 1996). Geological conditions, rock deformation experiments, and our FEM simulation results thus suggest that post-seismic-driven dislocation creep is a plausible deformation mechanism in the MAP.

One possible deformation mechanism that we did not investigate in this study is bulk cataclastic flow. Cataclastic flow, or brittle creep (not to be confused with fault creep attributed to afterslip), is a mesoscopic ductile behavior where deformation is accommodated by microscopic brittle processes, such as fracturing and frictional sliding along or across individual grains (Passchier & Trouw, 2013; Pluijm & Marshak, 2010). It occurs commonly within fault zones in the upper crust, where thermal condition and the effective normal stress between grains are low. Given the depth and temperature range of our lower wedge layer, it is possible that brittle creep could occur concurrently with our proposed dislocation creep during the post-seismic period. Previous studies, through both laboratory experiments and numerical simulations, have shown evidence supporting co-occurrence of cataclastic flow and plastic flow (Perfettini & Avouac, 2004; Reber et al., 2015; Tullis & Yund, 1987). Empirical laws describing the time-dependent stress-strain rate relationship for cataclastic flow have also been developed in the field of soil mechanics, and they generally suggest that strain rate is dependent on stress in the form of a power-law or exponential function (Mesri et al., 1981; Singh & Mitchell, 1968). However, a joint forward model considering contributions from cataclastic flow and viscoelastic relaxation is not a trivial task, as it involves integrating these constitutive relationships into the finite element modeling framework, which is beyond the scope of this study. Therefore, the findings of this study present a simple scenario where plastic flow is the sole mechanism resulting in the post-seismic deformation transients.

The presence of a viscous layer within accretionary prisms under low temperature condition has implications on the regional earthquake hazard potential, long-term structural evolution, and hydrocarbon formations. For instance, Onishi et al. (2001), Onishi and Kimura (1995) observed evidence for low temperature plastic flow that are associated with the mélange formation in the Shimanto Belt, an ancient accretionary complex in southwest Japan. Neglecting the viscous effects of the accretionary prism may also lead to biases in estimating the regional seismic hazard potential, as plate coupling model are commonly inverted from interseismic GPS observations into "back-slip" on the plate interface under the assumption of pure elastic wedge rheology. Here, we conducted

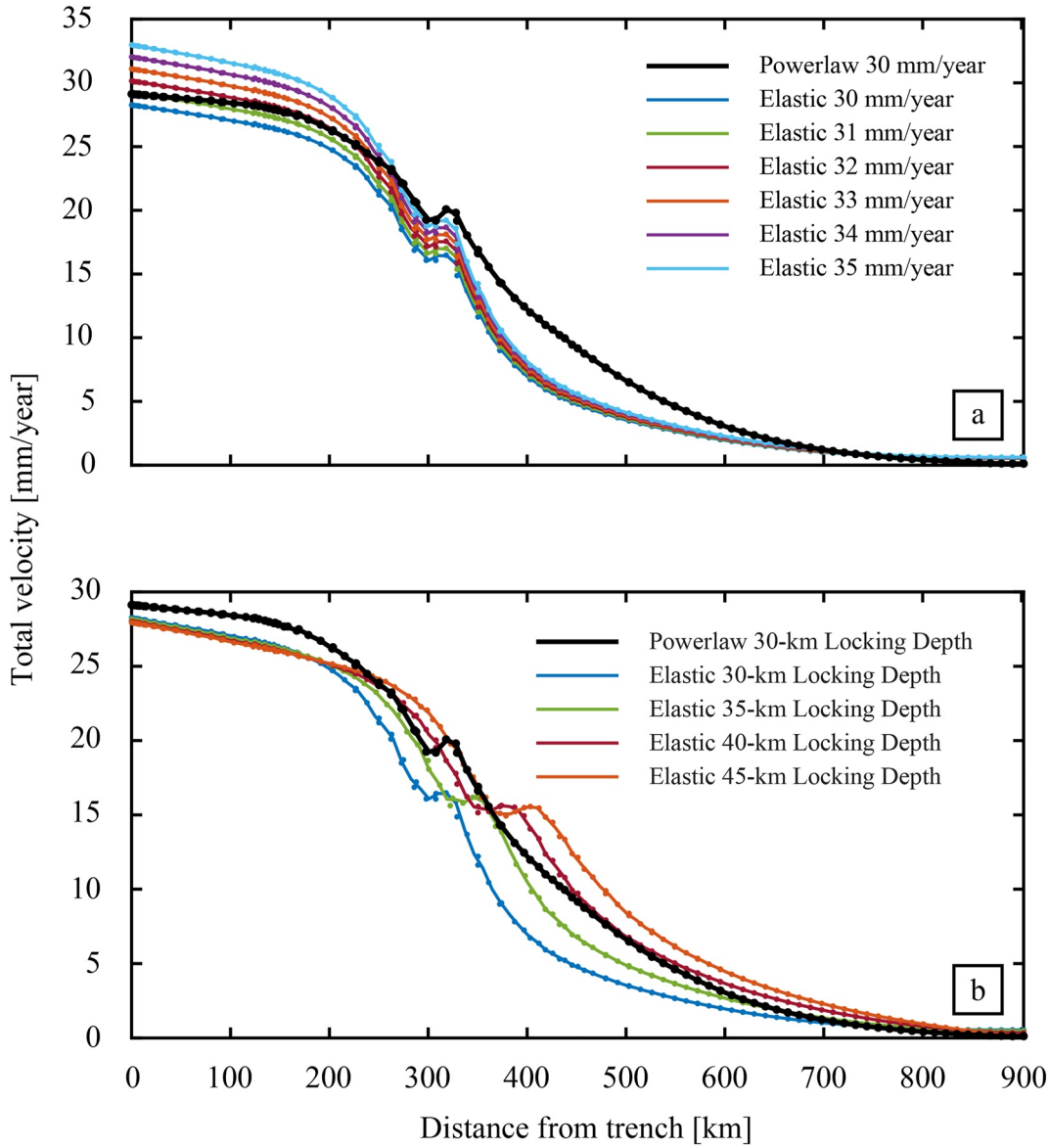

Figure 8. Forward-modeled trench-normal profiles of total surface velocity after 200 years of interseismic loading. (a) Models with varying back-slip rate but fixed locking depth of 30 km. (b) Models with varying locking depths but fixed back-slip rate of 30 mm/year. Black solid line: reference model assuming power-law lower wedge rheology. Colored lines: models with elastic lower wedge.

a series of simple forward back-slip models to illustrate how the wedge rheology can affect interseismic locking estimation. We first constructed a 3-D subduction zone geometry similar to our post-seismic relaxation model that includes the entire Arabic oceanic slab (Hayes et al., 2018). We assigned power-law viscoelastic rheology to the lower wedge using the estimated flow law parameters. We kept the upper wedge and oceanic slab to be elastic and the mantle to exhibit linear Maxwell rheology. We prescribed a constant 30 mm/year back-slip rate on the top of the slab above 30 km depth and drove the model for 200 years, after which we calculated the last-year surface velocities. We set this model to be the reference model. We then followed the same procedures but assigned the lower wedge to be elastic, and varied both the back-slip rate and the locking depth. We compared the last-year surface velocities from these elastic forward models to the reference viscous model, and the results are shown in Figure 8. We found that, in the case of the Makran, if the assumption of viscous lower wedge is valid, elastic wedge models tend to slightly overestimate the degree of locking (back-slip rate) of the megathrust (Figure 8a), and significantly overestimate the locking depth (Figure 8b). We also found that, when fixing the locking depth,

a viscous wedge model produces an interseismic surface velocity pattern with longer spatial wavelength than the elastic model. Although further analysis with comparison to interseismic GNSS data is needed to validate these potential effects, our modeling results are consistent with previous subduction zone interseismic studies assuming viscous continental mantle (Li et al., 2015, 2018; Wang et al., 2012).

5. Conclusions

The increasing volume of InSAR observations has allowed for monitoring post-seismic deformation following large earthquakes with high spatial and temporal resolution. Using the 2013 Baluchistan earthquake as an example, we are able to constrain the rheology structure and flow-law parameters within the Makran accretionary prism combining geodetic time-series analysis and numerical modeling techniques. Our finding of a partially viscous accretionary prism holds implications for reevaluating the seismic and tsunami hazard potential in the region, as well as conventional wedge mechanical models invoking linear-elasticity, such as the dislocation Okada solution. However, the Makran accretionary prism is a relatively rare case where the wedge is mostly exposed subaerially, and the desert environment is ideal for InSAR observation. To investigate the rheological properties of other accretionary prisms, future implementation of sea floor geodetic measurements for submarine wedges may help to determine whether the non-linear behavior of the Makran wedge occurs ubiquitously. In short, we make several valuable conclusions from our investigation of the post-seismic deformation following the 2013 Baluchistan earthquake:

1. Non-linear viscoelastic relaxation of an earthquake stress-induced, low-viscosity zone within the lower Makran accretionary prism (12–40 km deep) contributes to the 6.5-year post-seismic deformation following the 2013 Baluchistan earthquake.
2. A transient low-viscosity zone forms along the interface between the Makran accretionary prism and subducted slab, and relaxation of this zone likely contributes surface deformation that was interpreted by others as post-seismic afterslip on the slab interface.
3. The elastic-crystal plastic transition depth in the Makran subduction zone likely lies between 8- and 12-km depth. This is in consistent with the field observations of a common decollement near 10-km depth.
4. The estimated flow-law parameters of the lower Makran wedge ($n = 3.76 \pm 0.39$, $Q = 82.2 \pm 37.73$ kJ mol^{-1}, and $A = 10^{-3.36 \pm 4.69}$) suggest that the dominating deformation mechanism is likely low-temperature dislocation creep of fluid-saturated siliciclastics.
5. The presence of a partially viscous accretionary prism affects the estimation of seismic hazard potential in the region. Conventional elastic models tend to overestimate the locking depth and locking ratio when viscoelastic effects are neglected. These findings are consistent with previous subduction zone interseismic studies.

Data Availability Statement

The Sentinel-1 data used to generate post-seismic InSAR time-series was downloaded from Alaska Satellite Facility (ASF) Data Search Vertex (https://search.asf.alaska.edu/%23/). Several figures were generated using the Generic Mapping Tool (Wessel et al., 2013). The mesh geometry, preferred power-law model, and raw InSAR time-series are available as data supplements to this paper through Zenodo (https://doi.org/10.5281/zenodo.7227610).

Acknowledgments
The authors thank Editor Paul Tregoning, associate editor Yosuke Aoki, reviewers Tianhaozhe Sun and Kathryn Materna, and one anonymous reviewer whose suggestions greatly improved this manuscript. The authors thank Brad Aagaard and Charles Williams for providing generous technical supports on the PyLith software. We also thank Yage Zhu and Faqi Diao for supports on calculating the effective viscosity. This work was supported by NSF Award EAR 1917500. High-performance computational resources provided by the University of Iowa, Iowa City. Any use of trade, firm, or product names is for descriptive purposes only and does not imply endoresement by the U.S. Government.

References

Aagaard, B. T., Knepley, M. G., & Williams, C. A. (2013). A domain decomposition approach to implementing fault slip in finite-element models of quasi-static and dynamic crustal deformation. *Journal of Geophysical Research: Solid Earth*, *118*(6), 3059–3079. https://doi.org/10.1002/jgrb.50217

Abdollahi, S., Ardestani, V. E., Zeyen, H., & Shomali, Z. H. (2018). Crustal and upper mantle structures of Makran subduction zone, SE Iran by combined surface wave velocity analysis and gravity modeling. *Tectonophysics*, *747*, 191–210. https://doi.org/10.1016/j.tecto.2018.10.005

Ahmed, S. S. (1969). Tertiary geology of part of south Makran, Baluchistan, west Pakistan1. *AAPG Bulletin*, *53*(7), 1480–1499. https://doi.org/10.1306/5D25C863-16C1-11D7-8645000102C1865D

Avouac, J.-P., Ayoub, F., Wei, S., Ampuero, J.-P., Meng, L., Leprince, S., et al. (2014). The 2013, Mw 7.7 Balochistan earthquake, energetic strike-slip reactivation of a thrust fault. *Earth and Planetary Science Letters*, *391*, 128–134. https://doi.org/10.1016/j.epsl.2014.01.036

Barnhart, W. D., Hayes, G. P., Briggs, R. W., Gold, R. D., & Bilham, R. (2014). Ball-and-socket tectonic rotation during the 2013 Mw7.7 Balochistan earthquake. *Earth and Planetary Science Letters*, *403*, 210–216. https://doi.org/10.1016/j.epsl.2014.07.001

Bevis, M., Kendrick, E., Smalley, R., Jr., Brooks, B., Allmendinger, R., & Isacks, B. (2001). On the strength of interplate coupling and the rate of back arc convergence in the central Andes: An analysis of the interseismic velocity field. *Geochemistry, Geophysics, Geosystems*, *2*(11). https://doi.org/10.1029/2001GC000198

Burg, J.-P. (2018). Geology of the onshore Makran accretionary wedge: Synthesis and tectonic interpretation. *Earth-Science Reviews*, *185*, 1210–1231. https://doi.org/10.1016/j.earscirev.2018.09.011

Bürgmann, R., & Dresen, G. (2008). Rheology of the lower crust and upper mantle: Evidence from rock mechanics, geodesy, and field observations. *Annual Review of Earth and Planetary Sciences*, *36*(1), 531–567. https://doi.org/10.1146/annurev.earth.36.031207.124326

Burkhard, M. (1990). Ductile deformation mechanisms in micritic limestones naturally deformed at low temperatures (150–350°C). *Geological Society, London, Special Publications*, *54*(1), 241–257. https://doi.org/10.1144/GSL.SP.1990.054.01.23

Byrne, D. E., Sykes, L. R., & Davis, D. M. (1992). Great thrust earthquakes and aseismic slip along the plate boundary of the Makran Subduction Zone. *Journal of Geophysical Research*, *97*(B1), 449–478. https://doi.org/10.1029/91JB02165

Chlieh, M., Perfettini, H., Tavera, H., Avouac, J.-P., Remy, D., Nocquet, J.-M., et al. (2011). Interseismic coupling and seismic potential along the Central Andes subduction zone. *Journal of Geophysical Research*, *116*(B12), B12405. https://doi.org/10.1029/2010JB008166

Craig, T. J., & Copley, A. (2014). An explanation for the age independence of oceanic elastic thickness estimates from flexural profiles at subduction zones, and implications for continental rheology. *Earth and Planetary Science Letters*, *392*, 207–216. https://doi.org/10.1016/j.epsl.2014.02.027

Dahlen, F. A., Suppe, J., & Davis, D. (1984). Mechanics of fold-and-thrust belts and accretionary wedges: Cohesive Coulomb Theory. *Journal of Geophysical Research*, *89*(B12), 10087–10101. https://doi.org/10.1029/JB089iB12p10087

Davis, D., Suppe, J., & Dahlen, F. A. (1983). Mechanics of fold-and-thrust belts and accretionary wedges. *Journal of Geophysical Research*, *88*(B2), 1153–1172. https://doi.org/10.1029/JB088iB02p01153

DeMets, C., Gordon, R. G., & Argus, D. F. (2010). Geologically current plate motions. *Geophysical Journal International*, *181*(1), 1–80. https://doi.org/10.1111/j.1365-246X.2009.04491.x

Ellouz-Zimmermann, N., Lallemant, S., Castilla, R., Mouchot, N., Leturmy, P., Battani, A., et al. (2007). Offshore frontal part of the Makran accretionary prism: The Chamak survey (Pakistan) (pp. 351–366). https://doi.org/10.1007/978-3-540-69426-7_18

Fattahi, H. (2015). *Geodetic imaging of tectonic deformation with InSAR*. Ph.D., University of Miami. Retrieved from http://www.proquest.com/docview/1718489348/abstract/E100B091BDA34DF5PQ/1

Fowler, S. R., White, R. S., & Louden, K. E. (1985). Sediment dewatering in the Makran accretionary prism. *Earth and Planetary Science Letters*, *75*(4), 427–438. https://doi.org/10.1016/0012-821X(85)90186-4

Freed, A. M., & Bürgmann, R. (2004). Evidence of power-law flow in the Mojave Desert mantle. *Nature*, *430*, 6999. https://doi.org/10.1038/nature02784

Freed, A. M., Bürgmann, R., Calais, E., Freymueller, J., & Hreinsdóttir, S. (2006). Implications of deformation following the 2002 Denali, Alaska, earthquake for postseismic relaxation processes and lithospheric rheology. *Journal of Geophysical Research*, *111*(B1), B01401. https://doi.org/10.1029/2005JB003894

Frohling, E., & Szeliga, W. (2016). GPS constraints on interplate locking within the Makran subduction zone. *Geophysical Journal International*, *205*(1), 67–76. https://doi.org/10.1093/gji/ggw001

Fruehn, J., White, R. S., & Minshull, T. A. (1997). Internal deformation and compaction of the Makran accretionary wedge. *Terra Nova*, *9*(3), 101–104. https://doi.org/10.1046/j.1365-3121.1997.d01-13.x

Gleason, G. C., & Tullis, J. (1995). A flow law for dislocation creep of quartz aggregates determined with the molten salt cell. *Tectonophysics*, *247*(1), 1–23. https://doi.org/10.1016/0040-1951(95)00011-B

Griggs, D. T., & Blacic, J. D. (1965). Quartz: Anomalous weakness of synthetic crystals. *Science*, *147*(3655), 292–295. https://doi.org/10.1126/science.147.3655.292

Harms, J. C., Cappel, H. N., & Francis, D. C. (1984). The Makran coast of Pakistan: Its stratigraphy and hydrocarbon potential. *Marine Geology and Oceanography of Arabian Sea and Coastal Pakistan*, *3*(27).

Hayes, G. P., Moore, G. L., Portner, D. E., Hearne, M., Flamme, H., Furtney, M., & Smoczyk, G. M. (2018). Slab2, a comprehensive subduction zone geometry model. *Science*, *362*(6410), 58–61. https://doi.org/10.1126/science.aat4723

Heidarzadeh, M., & Satake, K. (2015). New insights into the source of the Makran tsunami of 27 November 1945 from tsunami waveforms and coastal deformation data. *Pure and Applied Geophysics*, *172*(3), 621–640. https://doi.org/10.1007/s00024-014-0948-y

Hirth, G., & Kohlstedt, D. (2003). Rheology of the upper mantle and the mantle wedge: A view from the experimentalists. In J. Eiler (Ed.), *Geophysical monograph series* (Vol. 138, pp. 83–105). American Geophysical Union. https://doi.org/10.1029/138GM06

Hirth, G., Teyssier, C., & Dunlap, J. W. (2001). An evaluation of quartzite flow laws based on comparisons between experimentally and naturally deformed rocks. *International Journal of Earth Sciences*, *90*(1), 77–87. https://doi.org/10.1007/s005310000152

Jackson, J., & McKenzie, D. (1984). Active tectonics of the Alpine–Himalayan belt between Western Turkey and Pakistan. *Geophysical Journal of the Royal Astronomical Society*, *77*(1), 185–264. https://doi.org/10.1111/j.1365-246X.1984.tb01931.x

Jaiswal, R. K., Singh, A. P., & Rastogi, B. K. (2009). Simulation of the Arabian sea tsunami propagation generated due to 1945 Makran earthquake and its effect on Western parts of Gujarat (India). *Natural Hazards*, *48*(2), 245–258. https://doi.org/10.1007/s11069-008-9261-3

Jaoul, O., Tullis, J., & Kronenberg, A. (1984). The effect of varying water contents on the creep behavior of Heavitree quartzite. *Journal of Geophysical Research*, *89*(B6), 4298–4312. https://doi.org/10.1029/JB089iB06p04298

Jolivet, R., Duputel, Z., Riel, B., Simons, M., Rivera, L., Minson, S. E., et al. (2014). The 2013 Mw 7.7 Balochistan earthquake: Seismic potential of an accretionary WedgeShort note. *Bulletin of the Seismological Society of America*, *104*(2), 1020–1030. https://doi.org/10.1785/0120130313

Kennedy, L. A., & Logan, J. M. (1998). Microstructures of cataclasites in a limestone-on-shale thrust fault: Implications for low-temperature recrystallization of calcite. *Tectonophysics*, *295*(1), 167–186. https://doi.org/10.1016/S0040-1951(98)00119-X

Khan, M. A., & Raza, H. A. (1986). The role of geothermal gradients in hydrocarbon exploration in Pakistan. *Journal of Petroleum Geology*, *9*(3), 245–258. https://doi.org/10.1111/j.1747-5457.1986.tb00388.x

Li, S., Moreno, M., Bedford, J., Rosenau, M., & Oncken, O. (2015). Revisiting viscoelastic effects on interseismic deformation and locking degree: A case study of the Peru-north Chile subduction zone. *Journal of Geophysical Research: Solid Earth*, *120*(6), 4522–4538. https://doi.org/10.1002/2015JB011903

Li, S., Wang, K., Wang, Y., Jiang, Y., & Dosso, S. E. (2018). Geodetically inferred locking state of the cascadia megathrust based on a viscoelastic Earth model. *Journal of Geophysical Research: Solid Earth*, *123*(9), 8056–8072. https://doi.org/10.1029/2018JB015620

Lin, Y. N., Jolivet, R., Simons, M., Agram, P. S., Martens, H. R., Li, Z., & Lodi, S. H. (2015). High interseismic coupling in the Eastern Makran (Pakistan) subduction zone. *Earth and Planetary Science Letters*, *420*, 116–126. https://doi.org/10.1016/j.epsl.2015.03.037

Luan, F. C., & Paterson, M. S. (1992). Preparation and deformation of synthetic aggregates of quartz. *Journal of Geophysical Research*, *97*(B1), 301–320. https://doi.org/10.1029/91JB01748

Lv, X., Amelung, F., & Shao, Y. (2022). Widespread aseismic slip along the Makran megathrust triggered by the 2013 Mw 7.7 Balochistan earthquake. *Geophysical Research Letters*, *49*(6), e2021GL097411. https://doi.org/10.1029/2021GL097411

Maggi, A., Jackson, J. A., Priestley, K., & Baker, C. (2000). A re-assessment of focal depth distributions in southern Iran, the Tien Shan and northern India: Do earthquakes really occur in the continental mantle? *Geophysical Journal International*, *143*(3), 629–661. https://doi.org/10.1046/j.1365-246X.2000.00254.x

Mesri, G., Febres-Cordero, E., Shields, D. R., & Castro, A. (1981). Shear stress-strain-time behaviour of clays. *Géotechnique*, *31*(4), 537–552. https://doi.org/10.1680/geot.1981.31.4.537

Moreno, M., Rosenau, M., & Oncken, O. (2010). 2010 Maule earthquake slip correlates with pre-seismic locking of Andean subduction zone. *Nature*, *467*, 198–202. https://doi.org/10.1038/nature09349

Muto, J., Moore, J. D. P., Barbot, S., Iinuma, T., Ohta, Y., & Iwamori, H. (2019). Coupled afterslip and transient mantle flow after the 2011 Tohoku earthquake. *Science Advances*, *5*(9), eaaw1164. https://doi.org/10.1126/sciadv.aaw1164

Onishi, C. T., & Kimura, G. (1995). Change in fabric of melange in the Shimanto Belt, Japan: Change in relative convergence? *Tectonics*, *14*(6), 1273–1289. https://doi.org/10.1029/95TC01929

Onishi, C. T., Kimura, G., Hashimoto, Y., Ikehara-Ohmori, K., & Watanabe, T. (2001). Deformation history of tectonic melange and its relationship to the underplating process and relative plate motion: An example from the deeply buried Shimanto Belt, SW Japan. *Tectonics*, *20*(3), 376–393. https://doi.org/10.1029/1999TC001154

Passchier, C. W., & Trouw, R. A. J. (2013). *Microtectonics*. Springer Science & Business Media.

Peña, C., Heidbach, O., Moreno, M., Bedford, J., Ziegler, M., Tassara, A., & Oncken, O. (2020). Impact of power-law rheology on the viscoelastic relaxation pattern and afterslip distribution following the 2010 Mw 8.8 Maule earthquake. *Earth and Planetary Science Letters*, *542*, 116292. https://doi.org/10.1016/j.epsl.2020.116292

Perfettini, H., & Avouac, J.-P. (2004). Postseismic relaxation driven by brittle creep: A possible mechanism to reconcile geodetic measurements and the decay rate of aftershocks, application to the chi-chi earthquake, Taiwan. *Journal of Geophysical Research*, *109*(B2). https://doi.org/10.1029/2003JB002488

Peterson, K. E., Barnhart, W. D., & Li, S. (2018). Viscous accretionary prisms: Viscoelastic relaxation of the Makran accretionary prism following the 2013 Baluchistan, Pakistan earthquake. *Journal of Geophysical Research: Solid Earth*, *123*(11), 10107–10123. https://doi.org/10.1029/2018JB016057

Platt, J. P., Leggett, J. K., Young, J., Raza, H., & Alam, S. (1985). Large-scale sediment underplating in the Makran accretionary prism, southwest Pakistan. *Geology*, *13*(7), 507–511. https://doi.org/10.1130/0091-7613(1985)13<507:lsuitm>2.0.co;2

Pluijm, B. A. V. D., & Marshak, S. (2010). *Earth structure: An introduction to structural geology and tectonics*. W.W. Norton.

Pollitz, F. F., Bürgmann, R., & Banerjee, P. (2006). Post-seismic relaxation following the great 2004 Sumatra-Andaman earthquake on a compressible self-gravitating Earth. *Geophysical Journal International*, *167*(1), 397–420. https://doi.org/10.1111/j.1365-246X.2006.03018.x

Post, A. D., Tullis, J., & Yund, R. A. (1996). Effects of chemical environment on dislocation creep of quartzite. *Journal of Geophysical Research*, *101*(B10), 22143–22155. https://doi.org/10.1029/96JB01926

Reber, J. E., Lavier, L. L., & Hayman, N. W. (2015). Experimental demonstration of a semi-brittle origin for crustal strain transients. *Nature Geoscience*, *8*(9), 715. https://doi.org/10.1038/ngeo2496

Rosen, P. A., Hensley, S., Peltzer, G., & Simons, M. (2004). Updated repeat orbit interferometry package released. *Eos, Transactions American Geophysical Union*, *85*(5), 47. https://doi.org/10.1029/2004EO050004

Rybacki, E., Gottschalk, M., Wirth, R., & Dresen, G. (2006). Influence of water fugacity and activation volume on the flow properties of fine-grained anorthite aggregates. *Journal of Geophysical Research*, *111*(B3). https://doi.org/10.1029/2005JB003663

Ryder, I., Parsons, B., Wright, T. J., & Funning, G. J. (2007). Post-seismic motion following the 1997 Manyi (Tibet) earthquake: InSAR observations and modelling. *Geophysical Journal International*, *169*(3), 1009–1027. https://doi.org/10.1111/j.1365-246X.2006.03312.x

Schlüter, H. U., Prexl, A., Gaedicke, C., Roeser, H., Reichert, C., Meyer, H., & von Daniels, C. (2002). The Makran accretionary wedge: Sediment thicknesses and ages and the origin of mud volcanoes. *Marine Geology*, *185*(3), 219–232. https://doi.org/10.1016/S0025-3227(02)00192-5

Shad Manaman, N., Shomali, H., & Koyi, H. (2011). New constraints on upper-mantle S-velocity structure and crustal thickness of the Iranian plateau using partitioned waveform inversion. *Geophysical Journal International*, *184*(1), 247–267. https://doi.org/10.1111/j.1365-246X.2010.04822.x

Singh, A., & Mitchell, J. K. (1968). General stress-strain-time function for soils. *Journal of the Soil Mechanics and Foundations Division*, *94*(1), 21–46. https://doi.org/10.1061/JSFEAQ.0001084

Snead, R. E. (1964). Active mud volcanoes of Baluchistan, west Pakistan. *Geographical Review*, *54*(4), 546–560. https://doi.org/10.2307/212981

Stipp, M., Stünitz, H., Heilbronner, R., & Schmid, S. M. (2002). The eastern Tonale fault zone: A 'natural laboratory' for crystal plastic deformation of quartz over a temperature range from 250 to 700°C. *Journal of Structural Geology*, *24*(12), 1861–1884. https://doi.org/10.1016/S0191-8141(02)00035-4

Sun, T., Wang, K., Iinuma, T., Hino, R., He, J., Fujimoto, H., et al. (2014). Prevalence of viscoelastic relaxation after the 2011 Tohoku-oki earthquake. *Nature*, *514*(7520), 84–87. https://doi.org/10.1038/nature13778

Tullis, J., & Yund, R. A. (1987). Transition from cataclastic flow to dislocation creep of feldspar: Mechanisms and microstructures. *Geology*, *15*(7), 606–609. https://doi.org/10.1130/0091-7613(1987)15<606:TFCFTD>2.0.CO;2

van Daalen, M., Heilbronner, R., & Kunze, K. (1999). Orientation analysis of localized shear deformation in quartz fibres at the brittle–ductile transition. *Tectonophysics*, *303*(1), 83–107. https://doi.org/10.1016/S0040-1951(98)00264-9

Wang, K., & Hu, Y. (2006). Accretionary prisms in subduction earthquake cycles: The theory of dynamic Coulomb wedge. *Journal of Geophysical Research*, *111*(B6). https://doi.org/10.1029/2005JB004094

Wang, K., Hu, Y., & He, J. (2012). Deformation cycles of subduction earthquakes in a viscoelastic Earth. *Nature*, *484*, 332. https://doi.org/10.1038/nature11032

Wenk, L., & Huhn, K. (2013). The influence of an embedded viscoelastic–plastic layer on kinematics and mass transport pattern within accretionary wedges. *Tectonophysics*, *608*, 653–666. https://doi.org/10.1016/j.tecto.2013.08.015

Wessel, P., Smith, W. H. F., Scharroo, R., Luis, J., & Wobbe, F. (2013). Generic mapping tools: Improved version released. *Eos, Transactions American Geophysical Union*, *94*(45), 409–410. https://doi.org/10.1002/2013EO450001

Wiedicke, M., Neben, S., & Spiess, V. (2001). Mud volcanoes at the front of the Makran accretionary complex, Pakistan. *Marine Geology*, *172*(1), 57–73. https://doi.org/10.1016/S0025-3227(00)00127-4

Yamasaki, T., & Houseman, G. A. (2012). The crustal viscosity gradient measured from post-seismic deformation: A case study of the 1997 Manyi (Tibet) earthquake. *Earth and Planetary Science Letters*, *351*(352), 105–114. https://doi.org/10.1016/j.epsl.2012.07.030

Zhang, Y., Fattahi, H., & Amelung, F. (2019). Small baseline InSAR time series analysis: Unwrapping error correction and noise reduction. *Computers & Geosciences*, *133*, 104331. https://doi.org/10.1016/j.cageo.2019.104331

Zhu, Y., Diao, F., Wang, R., Hao, M., Shao, Z., & Xiong, X. (2022). Crustal shortening and rheological behavior across the Longmen Shan Fault, eastern margin of the Tibetan Plateau. *Geophysical Research Letters*, *49*(11), e2022GL098814. https://doi.org/10.1029/2022GL098814

References From the Supporting Information

Christensen, N. I. (1996). Poisson's ratio and crustal seismology. *Journal of Geophysical Research*, *101*(B2), 3139–3156. https://doi.org/10.1029/95JB03446

Penney, C., Tavakoli, F., Saadat, A., Nankali, H. R., Sedighi, M., Khorrami, F., et al. (2017). Megathrust and accretionary wedge properties and behaviour in the Makran subduction zone. *Geophysical Journal International*, *209*(3), 1800–1830. https://doi.org/10.1093/gji/ggx126

Wang, K., He, J., Dragert, H., & James, T. S. (2001). Three-dimensional viscoelastic interseismic deformation model for the Cascadia subduction zone. *Earth Planets and Space*, *53*(4), 295–306. https://doi.org/10.1186/BF03352386